

A platinum@polymer-catechol nanobroker enables radio-immunotherapy for crippling melanoma tumorigenesis, angiogenesis, and radioresistance

Wenxi Li^{a,b,1}, Jie Yan^{a,b,1}, Hao Tian^{a,b}, Bei Li^{a,b}, Guohao Wang^{a,b}, Wei Sang^{a,b}, Zhan Zhang^{a,b}, Xuanjun Zhang^{a,b}, Yunlu Dai^{a,b,*}

^a Cancer Centre and Institute of Translational Medicine, Faculty of Health Sciences, University of Macau, Macau SAR, 999078, China

^b MOE Frontiers Science Center for Precision Oncology, University of Macau, Macau SAR, 999078, China

ARTICLE INFO

Keywords:

platinum@polymer-catechol nanobrokers
Melanoma PD-1:PD-L1 interaction blockade
Radio-sensitization effect
Anti-tumorigenesis
Anti-angiogenesis

ABSTRACT

Malignant melanoma cell-intrinsic PD-1:PD-L1 interaction thrusts tumorigenesis, angiogenesis, and radioresistance via mTOR hyperactivation to aggravate circumjacent aggression. Interdicting melanoma intrinsic growth signals, including the blockade of PD-L1 and mTOR signaling concurrently, cooperative with radiotherapy may provide a vigorous repertoire to alleviate the tumor encumbrance. Thence, we design a three-pronged platinum@polymer-catechol nanobroker to deliver mTOR inhibitor TAK228 and anti-PD-L1 antibody (aPD-L1) for impeding the melanoma-PD-1-driven aggression and maximizing the melanoma eradication. The aPD-L1 collaborated with TAK228 restrains melanoma cell-intrinsic PD-1: PD-L1 tumorigenic interaction via blocking melanoma-PD-L1 ligand and the melanoma-PD-1 receptor-driven mTOR signaling; corresponding downregulation of mTOR downstream protumorigenic cellular MYC and proangiogenic hypoxia-inducible factor 1-alpha is conducive to preventing tumorigenesis and angiogenesis, respectively. Further, high-Z metal platinum sensitizing TAK228-enhanced radiotherapy confers the nanobroker on remarkable tumoricidal efficacy. Hereto, the customized three-pronged nanobrokers efficiently suppress melanoma tumorigenesis and angiogenesis concomitant with the amplification of radiotherapeutic efficacy. Such an ingenious tactic may provide substantial benefits to clinical melanoma patients.

1. Introduction

Cutaneous malignant melanoma, derived from pigment-producing melanocytes, manifests rapid radial-growth concomitant with effortless dissemination to lymphatic or blood vessels [1–3], harshly threatening melanoma-bearing patients' survival quality and survival rate [4]. Conventional treatments, including chemotherapy and radiotherapy, are insufficient to conquer the stubbornness of advanced melanoma, which may be closely relevant to the melanoma intrinsic property. Unequivocally, Sonja Kleffel and his coworkers unveiled that melanoma cell-intrinsic PD-1:PD-L1 interaction overactivated the melanoma-PD-1 receptor-modulated downstream mammalian target of rapamycin (mTOR) signaling to accelerate the tumor aggression [5].

Mechanistically, hyperactivated mTOR (incorporating with other serviceable proteins or cytokines to function as mTORC1 and mTORC2) [6,7] is available to steer tumor aggression by manipulating general

transcription factors [8,9]. Specifically, mTORC2 induces the phosphorylation of protein kinase B (AKT) to increase the FoxO acetylation concomitant with FoxO phosphorylation inhibition [10,11], which cooperates with the mTORC1-mediated phosphorylation of translation repressor protein 4E-binding protein 1 (4E-BP1) to upregulate cellular MYC (cMYC) [12–16]. As a pivotal regulator in cell proliferation and metabolism, cMYC hyperactivation promotes tumorigenesis [9]. Meanwhile, the liberation of eukaryotic initiation factor 4E (eIF4E) also initiates the translation of hypoxia-inducible factor 1-alpha (HIF-1 α) and vascular endothelial growth factor (VEGF) [17,18], ultimately driving angiogenesis to support tumor growth and metastasis [19]. Furthermore, mTOR signaling is the prime compensatory pathway conferring melanoma resistance to radiotherapy [20,21]. Together, the melanoma cell-intrinsic PD-1:PD-L1 interaction hyperactivates mTOR signaling to instigate tumorigenesis, angiogenesis, and radioresistance. Accordingly, braking melanoma cell-intrinsic PD-1: PD-L1 protumorigenic interaction

Peer review under responsibility of KeAi Communications Co., Ltd.

* Corresponding author. Cancer Centre and Institute of Translational Medicine, Faculty of Health Sciences, University of Macau, Macau SAR, 999078, China.

E-mail address: yldai@um.edu.mo (Y. Dai).

¹ Wenxi Li and Jie Yan contributed equally to this work.

<https://doi.org/10.1016/j.bioactmat.2022.09.006>

Received 30 June 2022; Received in revised form 21 August 2022; Accepted 13 September 2022

2452-199X/© 2022 The Authors. Publishing services by Elsevier B.V. on behalf of KeAi Communications Co. Ltd. This is an open access article under the CC BY-NC-ND license (<http://creativecommons.org/licenses/by-nc-nd/4.0/>).

via combining mTOR inhibition with anti-PD-L1 antibody (aPD-L1) may produce a new repertoire to impede melanoma intrinsic tumor growth and melanoma-PD-L1:lymphocytes-PD-1 interaction-mediated immune evasion concurrently. Further, mTOR inhibition may increase the radiosensitivity of melanoma, thereby galvanizing durable tumor regression via enhancing tumor ablation and arousing tumoricidal immune responses.

In recent years, biological materials were widely explored to construct versatile nanoplatforms, thereby remedying the limitations of traditional modalities [22,23]. Natural or synthetic polyphenols are prevalent compounds for metal-coordination or noble metal reductants, and the oxidized polyphenols can serve as capping reagents to form and stabilize programmable nanocages. The feasible redox between diverse metals with high reduction potentials and phenolic donors endows nanocages with pleiotropic properties, including excellent biocompatibility and convenient manipulation [24–28]. Here, we tactfully designed a mTOR inhibitor TAK228-loaded aPD-L1-enriched platinum-based three-pronged platinum@polymer-catechol nanobraker (aPD-L1-Pt@TAK228@PEG-polyphenol, denoted as APTP NPs) with radio-reinforced tumoricidal-immunity for dampening melanoma intrinsic PD-1:PD-L1

protumorigenic signaling and enhancing the melanoma eradication (Fig. 1). Firstly, the amphiphilic polymer polyethylene glycol (PEG)-catechol enriching amide groups was synthesized as phenolic donors [29]. Subsequently, the amphiphilic PEG-catechol oxidized high-Z radiosensitizing platinum ions (Pt^{2+}) to Pt^0 and packed inhibitor TAK228 via metal redox reactions and hydrophobic interaction concurrently, forming pH-responsive platinum-based nanoparticles (named PTP NPs) [30–32]. Finally, the aPD-L1 was tactfully attached to the PTP NPs via electrostatic adsorption to obtain the three-pronged platinum@polymer-catechol nanobraker (APTP NPs), which could actively target PD-L1-overexpressed melanoma cells [33,34]. In this scenario, the combination of aPD-L1 and TAK228 dually interdicted melanoma cell-intrinsic PD-1:PD-L1 interaction via blocking melanoma-PD-L1 ligand and the melanoma-PD-1 receptor downstream mTOR signaling pathway. The blockage of mTOR restrained the tumor growth and metastasis via thwarting mTOR/AKT/cMYC axis-modulated tumorigenesis and mTORC1/HIF-1 α /VEGF axis-modulated angiogenesis. Meanwhile, the radiosensitizer Pt cooperated with TAK228 to enhance radiotherapy to expedite tumor destruction and promote neo-antigen presentation for arousing durable tumoricidal immune response

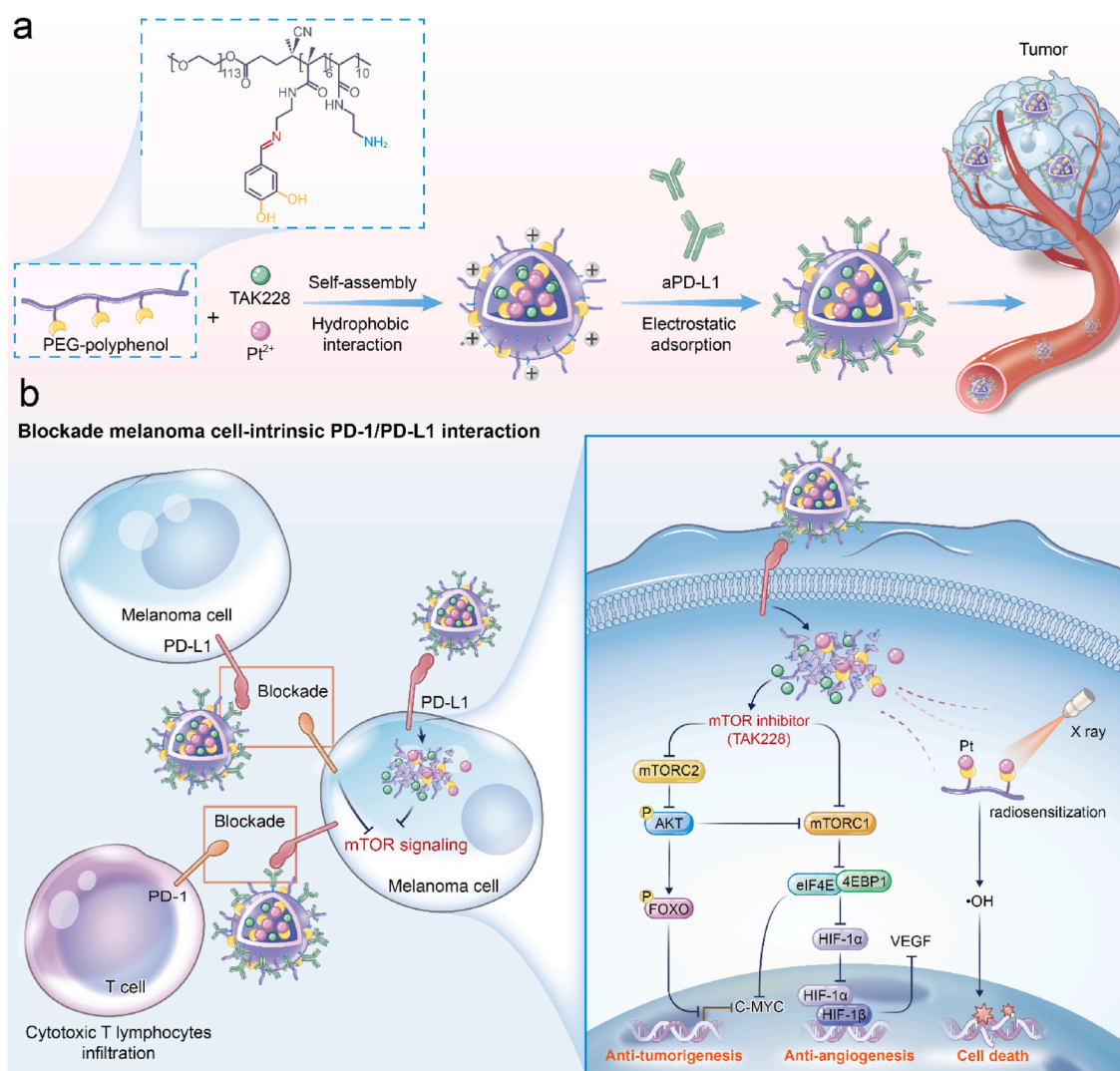


Fig. 1. The fabrication process and anti-tumor mechanism related to APTP nanobraker. **a** Schematic illustration of amphiphilic PEG-polyphenol-assisted assembly of APTP NPs. **b** Mechanism illustration of APTP NPs against melanoma-intrinsic tumor aggression. aPD-L1-adsorbed on the nanobraker actively target melanoma cells and blocking melanoma-PD-L1 receptor. Then, the loaded mTOR inhibitor TAK228 was released to intercede the melanoma cell-intrinsic PD-1/PD-L1 interaction via dampening protumorigenic mTOR pathway. The inhibition of mTOR signaling was beneficial to downregulate protumorigenic cMYC and proangiogenic HIF-1 α . Additionally, radiosensitizing high-Z metal Pt cooperating with TAK228 ameliorates radiotherapy to accelerate cell death. Besides, aPD-L1-adsorbed on the nanobraker blocked the lymphocyte-PD-1:melanoma-PD-L1 interaction to facilitate the effective infiltration of cytotoxic T lymphocytes.

[35,36]. The aPD-L1 attached on APTP NPs also facilitated the effective infiltration of cytotoxic T lymphocytes (CTLs) via blocking melanoma-PD-L1:lymphocyte-PD-1 interaction. Conclusively, this three-pronged platinum@polymer-catechol nanobroker may give a unique insight into the clinical treatment of melanoma.

2. Experimental methods

2.1. Materials

Anti-mouse PD-L1 (Purified in vivo) was purchased from Leinco. TAK228 was purchased from DC chemical. K_2PtCl_4 was purchased from Sigma-Aldrich. Repligen Biotech CE Dialysis Tubing Trial Kit-300KDa was purchased from Spectrum. Methylthiazolyldiphenyl-tetrazolium bromide, Crystal violet were purchased from Beyotime. Annexin V-FITC/7-AAD apoptosis kit was purchased from Solarbio. HCS DNA Damage Kit was purchased from Invitrogen™. All antibodies referring to Western blot assay were purchased from Cell Signaling Technology. Halt™ Protease and Phosphatase Inhibitor Cocktail (100X), Slide-A-Lyzer™ MINI Dialysis Device (3.5K MWCO, 2 mL) were purchased from Thermo Fisher Scientific. Amicon® Ultra-15 Centrifugal Filter Unit was purchased from Millipore. Flow Cytometry (FCM) Permeabilization/Wash Buffer I was purchased from R&D. DNase I was purchased from Roche. Collagenase (Type IV) powder was purchased from Gibco. All antibodies used in FCM were purchased from eBioscience. ELISA Kits was purchased from Neobioscience Technology Company. Recombinant murine IL-4, and animal-free recombinant murine GM-CSF were purchased from Pepro Tech.

2.2. Cell line and animals

B16F10 cell line was obtained from the cell bank of the Faculty of Health Science, University of Macau. B16F10 cells were cultured by Dulbecco's Modified Eagle's Medium/Nutrient Mixture F-12 Ham (DMEM/F-12) medium (Gibco) containing 10% fetal bovine serum (FBS) (Gibco) and 1% Penicillin-Streptomycin (100 $\mu\text{g mL}^{-1}$ streptomycin sulfate, 100 U mL^{-1} penicillin G sodium) in an incubator containing 5% CO_2 at 37 °C. Bone marrow-derived dendritic cells (BMDCs) were derived from bone marrows isolated from C57BL/6J female mouse (8–10 weeks old) thighbone according to an established protocol [37, 38] and cultured in RPMI 1640 medium with 10% FBS. C57BL/6J mice were purchased from the Animal Research Core of Faculty of Health Sciences, University of Macau. The animal research protocol (UMARE-030-2018) was approved by the University of Macau Animal Ethics Committee.

2.3. Synthesis of polyphenols polymer

Synthesis of monomer. N-Boc-ethylenediamine (3.2 g, 20 mmol) was dissolved in 50 mL anhydrous dichloromethane (DCM) with triethylamine (8.6 mL, 60 mmol), then methacryloyl chloride (2.3 mL, 24 mmol) was added dropwise at 0 °C in 1 h and stirred overnight at room temperature. Finally, the product was purified by column chromatography (eluent: $\text{CH}_2\text{Cl}_2/\text{CH}_3\text{OH}$, 1/1 v/v). Yield: 3.4 g (77%).

Synthesis of macromolecular initiator PEG-chain transfer agent (CTA). PEO227-OH (5.0 g, 0.50 mmol), 4-dimethylaminopyridine (DMAP) (0.012 g, 0.10 mmol), and the reversible addition-fragmentation chain transfer (RAFT) agent 4-cyano-4-(phenylcarbonothioylthio) pentanoic acid (CBPA) (0.15 g, 0.55 mmol) were all dissolved in 20 mL of DCM at 0 °C. Then, added the N, N'-dicyclohexylcarbodiimide (DCC) solution (0.21 g, 1.0 mmol) dropwise. The reaction was stirred at room temperature for 72 h. The final product was purified by precipitating in diethyl ether three times and dried in vacuo overnight. Yield: 4.8 g (93%).

Synthesis of polymer PEG-b-NH₂. PEG-CTA (0.20 g, 40 μmol), monomer (0.23 g, 1.0 mmol), and azobisisobutyronitrile (AIBN) (10 mg,

60 μmol) were used for a RAFT polymerization. The reaction was carried out at 90 °C for 4 h, then the polymer (PEG-b-PNH₂Boc) was got by precipitations in diethyl ether and dried in a vacuum overnight. Yield: 0.32 g (74%). Amino-functionalized polymer was got by using PEG-b-PNH₂Boc (0.32 g) solubilized in the dichloromethane (5 mL, 20% TFA) and stirred for 4 h to remove protecting groups. Yield: 0.22 g (85%).

Synthesis of PEG-polyphenol. Finally, a solution of PEG-b-NH₂ (0.22 g), 3,4-dihydroxybenzaldehyde (0.27 g, 2.0 mmol) in 20 mL CH_3OH was stirred under nitrogen at 60 °C for overnight to get the PEG-polyphenol. Yield: 0.28 g (58%).

2.4. Preparation of aPD-L1-Pt@TAK228@PEG-polyphenol (APTP) NPs

Firstly, 5 mg K_2PtCl_4 was dissolved in deionized water (DI water). 5 mg TAK228 and 5 mg PEG-polyphenol were dissolved in 1 mL methanol respectively. Add the mixture of 50 μL TAK228 (5 mg mL^{-1}) and 750 μL PEG-polyphenol (5 mg mL^{-1}) to the 4 mL DI water containing 150 μL K_2PtCl_4 (5 mg mL^{-1}) under the ultrasound, continuing the sonicate for 15 min. Methanol in the ultrasonic mixed solution was removed by rotary evaporator to obtain self-assembled nanoparticles (Pt@TAK228@PEG-polyphenol, designated as PTP NPs). Obtained PTP NPs were preliminarily purified by 10 KDa ultrafiltration tubes at 3500 rpm centrifugation speed for 10 min, followed by the dialysis (7 KDa) approximately 3 h. Subsequently, 140 μg aPD-L1 were rapidly added in the PTP NPs dispersive solution prepared above under the ultrasound for 10 min to obtain the aPD-L1-Pt@TAK228@PEG-polyphenol (APTP) NPs via electrostatic adsorption. Finally, the APTP NPs were purified by a 300 KDa dialysis bag and concentrated by 10 KDa ultrafiltration tubes for further use.

2.5. Characterization of APTP NPs

The morphology was investigated by a JEM-3010UHR/JEM-2100F field transmission electron microscopy (TEM). The elemental analysis of APTP NPs was detected by Energy dispersive X-ray spectroscopy (EDX) elemental mapping and spectra. The hydrodynamic diameter and the ζ potential were measured by a Malvern Zetasizer Nano ZSP system ZEN5600. The inductively coupled plasma mass spectrometry (ICP-MS) was utilized to evaluate the encapsulation rate of platinum. The calculation formula is as follows: Metal encapsulation rate (%) = (Encapsulated metal quality/Original metal quality) \times 100%. The electrostatic adsorption of aPD-L1 was detected by sodium dodecyl sulfate-polyacrylamide gel electrophoresis (SDS-PAGE) assay (6% gel), which was visualized by Coomassie Brilliant Blue G250. TAK228 concentration was determined by HPLC analysis in a gradient elution method: acetonitrile/ $\text{NH}_4\text{H}_2\text{PO}_4$ (0.01 mol mL^{-1}) (v/v) = 5:95 to 15:85 (40 min), 15:85 to 5:95 (40–50 min), 50:50 (10–12 min), flow rate = 1 mg mL^{-1} , detection wavelength = 247 nm.

2.6. Western blot assay

Total proteins under diverse treatments (PBS, TAK228, APTP NPs in vitro (TAK228, 50 nM, 12 h); PBS (+), TAK228 (+), APTP NPs (+) in vivo) were extracted from the B16F10 cells or tumor tissues with the protection of Protease and Phosphatase Inhibitor Cocktail. p-mTOR^{S2481} and VEGFR2 were separated using 6% SDS-PAGE; HIF-1 α and p-FOXO were separated using 10% SDS-PAGE; PD-L1, p-AKTS473, c-MYC, VEGF, and β -actin were separated using 12% SDS-PAGE, followed by the transfer onto polyvinylidene difluoride (PVDF) membranes. The obtained blots were blocked by 5% defatted milk at room temperature for 1 h and immediately incubated with the relevant primary antibodies (anti-p-mTOR^{S2481} antibody (1:1000), anti-VEGFR2 antibody (1:1000), anti-PD-L1 antibody (1:2000), anti-HIF-1 α antibody (1:1000), anti-p-FOXO antibody (1:1000), anti-p-AKTS473 antibody (1:1000), anti-cMYC antibody (1:1000), anti-VEGF antibody (1:1000), and anti- β -actin antibody (1:3000)) overnight at 4 °C, followed by the incubation

with anti-mouse or anti-rabbit IgG-HRP secondary antibodies at room temperature for 2 h. Finally, the corresponding protein bands were captured on BioRad ChemiDoc MP Imaging Systems.

2.7. Cytotoxicity, cell apoptosis and cell cycle assay

B16F10 cells were seeded in 96-well plates (5000 cells per well) for cytotoxicity assay or 6-well plates (2×10^5 cells per well) for cell apoptosis and cell cycle assay. After 12h, the B16F10 cells were treated with various drugs (PBS, PP, TAK228, PTP, APTP) and irradiated (or not) by X-ray irradiation (6 Gy), followed by another 24 h incubation to evaluate the cytotoxicity, cell apoptosis assay, and cell cycle. Cell viability was measured by the MTT assay. Cell apoptosis was detected by Annexin V-FITC/7-AAD Apoptosis Detection Kit according to the corresponding protocol. The treated cells were fixed and permeated with 75% ethyl alcohol after the disposal of RNase A, followed by the staining of propidium iodide to detect the cell cycle.

2.8. Cell internalization of APTP NPs

B16F10 cells were seeded in confocal dishes (2×10^5 cells per dish) and cultured overnight. On the next day, cells (with or without anti-PD-L1 antibody pre-blockage) were incubated with fluorescein PEG-IR780-fabricated PTP or APTP NPs for 6 h. Subsequently, all the treated cells were fixed by 4% paraformaldehyde solution and washed by PBS solution thoroughly, followed by the staining with DAPI for 10 min. Finally, cell internalization of APTP NPs was observed by a confocal laser scanning microscopy (CLSM, Carl Zeiss Confocal LSM710) and analyzed by Zen software.

2.9. X-ray induced DNA damage

B16F10 cells were seeded in confocal dishes (8×10^4 cells per dish) and cultured overnight, which were irradiated by X-ray at 6 Gy after the 6 h co-incubation with various drugs (PBS, PP, TAK228, PTP, APTP NPs). HCS DNA Damage Kit (Invitrogen) was used to determine DNA damage according to the corresponding protocol after another 30 min incubation. Briefly, the treated cells were fixed by 4% paraformaldehyde solution and permeabilized by 1% Triton-100 solution for 10 min, respectively. Afterward, the cells were exposed to a 5% BSA blocking solution for 1 h and further incubated with γ -H₂AX mouse monoclonal antibody for 1 h, followed by the staining of Alexa Fluor® 555 goat anti-mouse IgG (1:2000) for 1 h and Hoechst 33342 (1:6000) for 15 min at room temperature, respectively. The cells were washed three times with PBS at each step. Finally, the images were obtained by CLSM (Carl Zeiss Confocal LSM710).

2.10. Colony formation assay

The B16F10 cells were seeded in a 6-well culture plate at a density of 1000 cells per well and incubated for 24 h. Cells under various incubations (PBS, PP, TAK228, PTP, APTP NPs) were irradiated by X-ray for 6 Gy at 6 h. Maintaining another 5 days routine incubation, followed by the sequential fixation with 4% paraformaldehyde and staining with crystal violet to calculate the survival fraction by cloning cluster. The calculation formation as follows: Surviving fraction = (surviving colonies)/(cells seeded \times plating efficiency) \times 100%. Plating efficiency = number of colonies formed/number of cells inoculated \times 100%.

2.11. DCs maturation In vitro

Bone marrow-derived dendritic cells (BMDCs) were isolated from C57BL/6J female mouse (8–10 weeks old) thighbone according to an established protocol [37,38]. Briefly, after obtaining the sterile femurs and tibias, we flushed the bones repeatedly with RPMI 1640 medium to harvest bone marrow monocytes, followed by the digestion of ACK lysis

buffer to destroy red blood cells. Cells were cultured with the RPMI 1640 medium containing IL-4 (10 ng mL⁻¹) and GM-CSF (20 ng mL⁻¹) for 5 days. The cancer cells under various treatments were co-cultured with the BMDCs at the ratio of 1:1 for 24 h. The BMDCs without any treatment and with the LPS stimulation were regarded as negative and positive control, respectively. In the end, the relevant medium supernatants were collected for pro-inflammatory cytokines (TNF- α , IL-6, IL-12p70) detection via ELISA kits, and the BMDCs under various treatments were collected to evaluate the in vitro DCs maturation (CD11c⁺ CD80⁺ CD86⁺, gated on CD11c⁺ DCs) by a flow cytometry (BD ACCURI C6).

2.12. Tumor therapeutic performance of APTP NPs in vivo

For the validation of tumor therapeutic performance of APTP NPs, we firstly established a bilateral subcutaneous B16F10 tumor-bearing C57BL/6J female mice model by injecting 1×10^6 cells into the left flank as primary tumor and 0.5×10^6 cells into the right flank as distant tumor. When the primary tumor volume increased to circa 150 mm³ at 10 days and the distant tumor volume reached \sim 80 mm³, the mice were divided into 6 groups (4 mice per group) including PBS (-), PBS (+), PP (+), TAK228 (+), PTP (+), and APTP (+). Afterward, the primary tumor sustained the X-ray irradiation for 6 Gy at the 12-h point post diverse i.v. administration (Drug concentration per mouse: Pt (166 μ g), TAK228 (155 nM), and aPD-L1 antibody (46.7 μ g)). The treatment loop was executed three consecutive times (0, 2nd, and 4th day), concomitant with the monitor of tumor volume variations and body weight every other day. All treated mice were euthanized to harvest tumors for further analysis on the tenth day. The sera were collected for biochemistry analysis.

For assessing the impact of APTP NPs on the mice survival rate, we changed the animal model into the lateral subcutaneous B16F10 tumor-bearing C57BL/6J female mice model via inoculating 1×10^6 cancer cells into the left flank. When the primary tumor volume increased to circa 150 mm³ at 10 days, same treatment procedure as therapeutic experiment was executed concomitant with the tumor volume monitoring frequency every four days. All treated mice were euthanized once the tumor volume exceeded the stipulation (\sim 2000 mm³).

2.13. Flow cytometric evaluation of immunological effect by APTP NPs

A bilateral subcutaneous B16F10 tumor-bearing C57BL/6J female mice model was reestablished and conducted the same therapeutic procedure as the anti-tumor therapeutic experiment to verify the immunological deployment capacity of our nanobroker APTP NPs. The mice bore various treatments were euthanized on the 10th day to collect sera for cytokines detection (IL-6, IFN- γ , TNF- α) and to harvest tumors, spleens, and lymph nodes for immunological analysis. In detail, the harvested tumors were cut into diminutive tissues and digested by dissociation buffer containing hyaluronidase (100 U), deoxyribonuclease (100 mg mL⁻¹) and collagenase IV (1 mg mL⁻¹) for 90 min at 37 °C, followed by the homogenization into suspended single cells. Spleens and lymph nodes were directly homogenized into suspended single cells. All the red blood cells in the single-cell suspensions mentioned above was lysed by the ACK lysis buffer. Then the relevant suspended single cells were fixed and permeabilized by Flow Cytometry Permeabilization/Wash Buffer I.

For the immunological analysis, the cells were stained with corresponding antibodies: CD11c (eBioscience, Cat No. 11-0114-81, dilution ratio 1:100), CD86 (eBioscience, Cat No. 12-0862-81, dilution ratio 1:100), CD80 (eBioscience, Cat No. 17-0801-82, dilution ratio 1:100), CD3e (eBioscience, Cat No. 11-0031-82, dilution ratio 1:50), CD8a (eBioscience, Cat No. 45-0081-82, dilution ratio 1:50), Ki67 (Biolegend, Cat No. 652411, dilution ratio 1:100), Granzyme B (Biolegend, Cat No. 652411, dilution ratio 1:50), CD45 (eBioscience, Cat No. 11-0451-82, dilution ratio 1:50), CD3e (eBioscience, Cat No. 12-0031-83, dilution

ratio 1:50), CD4 (eBioscience, Cat No. 25-0042-82, dilution ratio 1:50), CD62L (eBioscience, Cat No. 17-0621-83, dilution ratio 1:100), CD44 (eBioscience, Cat No. 12-0441-81, dilution ratio 1:100) according to the manufacturer's instructions. After staining, the cells were washed by FACS buffer and resuspended in FACS buffer and analyzed by the flow cytometry (FCM, Beckman CytoFLEX S Flow Cytometer). The data were analyzed using FlowJo 10.0.

2.14. Statistical analysis

Software GraphPad Prism 7.00 was used for the data analysis. Differences between groups were determined by ordinary one-way ANOVA analysis and Tukey's multiple comparison test. Statistical significance was defined as * $p < 0.05$, ** $p < 0.01$, *** $p < 0.001$, **** $p < 0.0001$. Data were presented as mean \pm SD.

3. Results

3.1. Synthesis and characterization of APTP

Emerging evidence revealed that melanoma-PD-1 expression promoted tumor growth and tumorigenesis via melanoma cell-intrinsic PD-1:PD-L1 interaction [5]. The expression of PD-1 and PD-L1 in a murine melanoma cell line (B16F10) were verified via confocal laser scanning microscopy (CLSM) imaging, flow cytometry (FCM) analyses, and Western blot detections (Fig. S1). Interferon- γ (IFN- γ) was added into the culture medium to potentiate PD-L1 expression for investigating the tumor targeting and PD-L1 blockade capability of aPD-L1-modified nanoparticles [39]. B16F10 cells expressed approximately $50.6 \pm$

1.6% PD-L1 on the cell membrane, even increased to $99.8 \pm 0.5\%$ within the stimulation of IFN- γ , which may aggravate immune evasion. Simultaneously, around $6.5 \pm 0.7\%$ PD-1 was expressed on B16F10 cells, suggesting the potential of melanoma-PD-1 mediated tumor aggression. To fabricate an innovative nanobreaker for overcoming melanoma intrinsic tumorigenesis and melanoma-PD-L1: lymphocytes-PD-1 interaction-mediated immune evasion, an amphiphilic polymer@catechol (PEG-polyphenol) was synthesized as a carrier. The proton nuclear magnetic resonance (^1H NMR) spectra of intermediate products PEG-b-NH $_2$ (Fig. S2), 3,4-dihydroxybenzaldehyde (Fig. S3), and end-product PEG-polyphenol (Fig. S4) were utilized to prove the successful synthesis. The obtained PEG-polyphenol was endowed with versatile properties by diverse groups, including metal redox by polyphenol structure [40], protein adsorption via electropositive amino groups [41], and pH responsiveness via imine bonds (Fig. 2a) [42]. TAK228 and Pt $^{2+}$ ions were self-assembled with amphiphilic PEG-polyphenol via a handy ultrasonication to form PTP NPs, whose further encasement with aPD-L1 in virtue of electrostatic adsorption produced aPD-L1-functionalized spherical APTP NPs (Fig. 2b). The elemental platinum, sulfur, carbon, nitrogen, and oxygen were distributed in APTP NPs symmetrically, confirming the successful platinum chelation and aPD-L1 modification (Fig. 2c and d). The encapsulation rate and drug loading efficiency of Pt in APTP NPs determined by inductively coupled plasma mass spectrometry (ICP-MS) were $66.22 \pm 0.36\%$ and $10.96 \pm 0.06\%$, respectively (Table S1 and Fig. S5). The encapsulation efficiency and drug loading efficiency of TAK228 in APTP NPs were 57.2% and 3.16%, respectively. The hydrodynamic size of PTP and APTP NPs was 78.82 ± 4.8 nm and 105.7 ± 6.5 nm, respectively (Fig. 2e). The acceptable size variation of APTP NPs

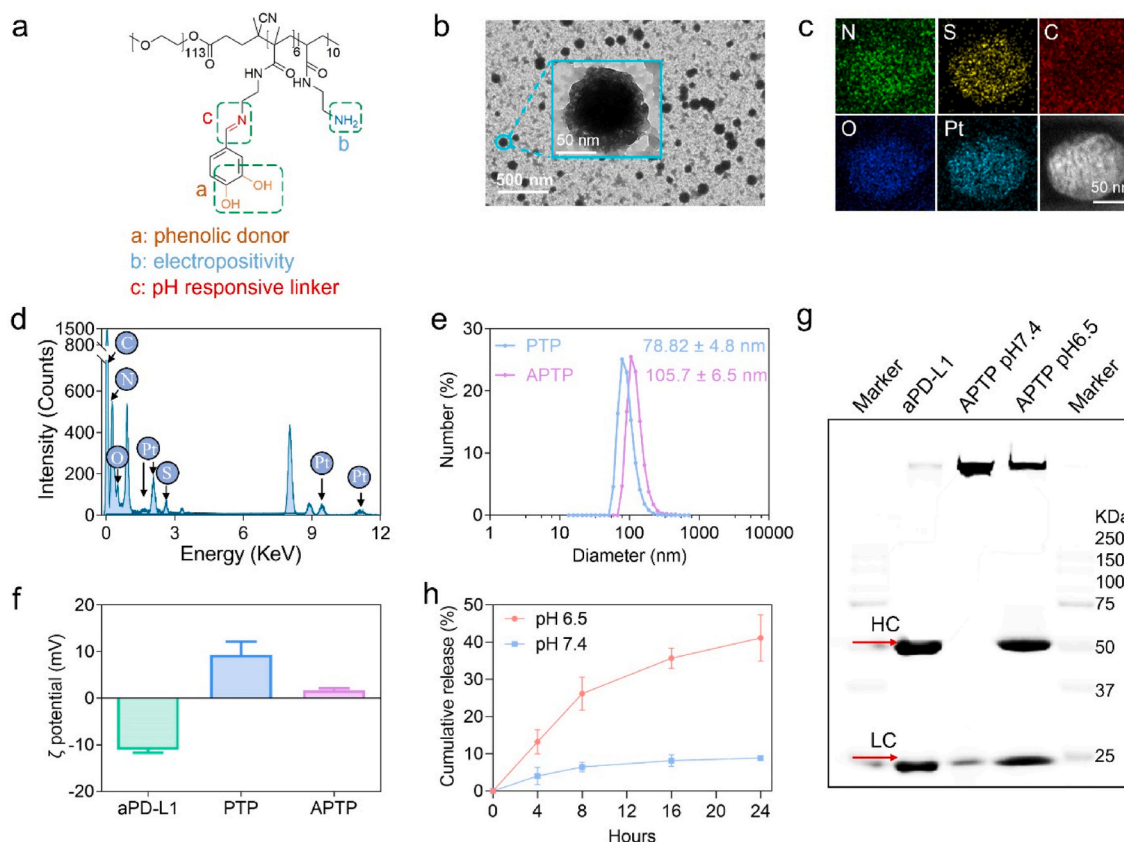


Fig. 2. Characterizations of APTP NPs. **a** Illustration of the structure of the amphiphilic PEG-polyphenol. **b** Transmission electron microscope (TEM) image of aPD-L1-functionalized APTP NPs. The inserted picture illustrates the enlarged morphology of APTP NPs. **c,d** Energy-dispersive X-ray spectroscopy (EDX) elemental mapping and spectra of APTP NPs. **e** Dynamic light scattering (DLS) of PTP and APTP NPs. **f** ζ potential analyses of aPD-L1, PTP, and APTP NPs. **g** SDS-PAGE image of aPD-L1 and APTP NPs under the different pH. 'HC' represents high chains, 'LC' represents light chains. **h** The pH-responsive release profile of APTP NPs using fluorochrome Nile red as a model drug.

incubated in H₂O, phosphate-buffered saline (PBS, pH = 7.4), and DMEM/F-12 medium for 72 h revealed reliable stability of APTP NPs (Fig. S6). The zeta potential of aPD-L1-functionalized APTP NPs declined from 9.3 mV (PTP NPs) to 1.7 mV attributing to the negative charge of aPD-L1 (Fig. 2f). Additionally, the protein retardation of APTP lane at pH 7.4 ascertained the successful adsorption of aPD-L1 on PTP NPs through sodium dodecyl sulfate-polyacrylamide gel electrophoresis (SDS-PAGE) assay (Fig. 2g). The pH-responsive release of aPD-L1 was validated at SDS-PAGE assay concurrently on account of partial band-shift of aPD-L1 in APTP lane within acidic solution (pH 6.5). A hydrophobic fluorochrome Nile red instead of TAK228 was encapsulated into APTP NPs to reconfirm the pH-responsive disassembly

profiles, demonstrating that approximately 40% of the model drug was liberated within 24 h at pH 6.5 while being inferior to 10% at pH 7.4 (Fig. 2h and Fig. S7) [43]. Collectively, a pH-responsive aPD-L1-functionalized TAK228-loaded platinum@polymer-catechol nanobroker was successfully fabricated for impeding melanoma-PD-1-driven tumor invasion.

3.2. In vitro evaluation of APTP NPs-mediated active targeting and tumor cell inhibition

Prior to the investigation of tumoricidal potential, the active targeting potentiality of nanobroker to tumor cells was scrupulously

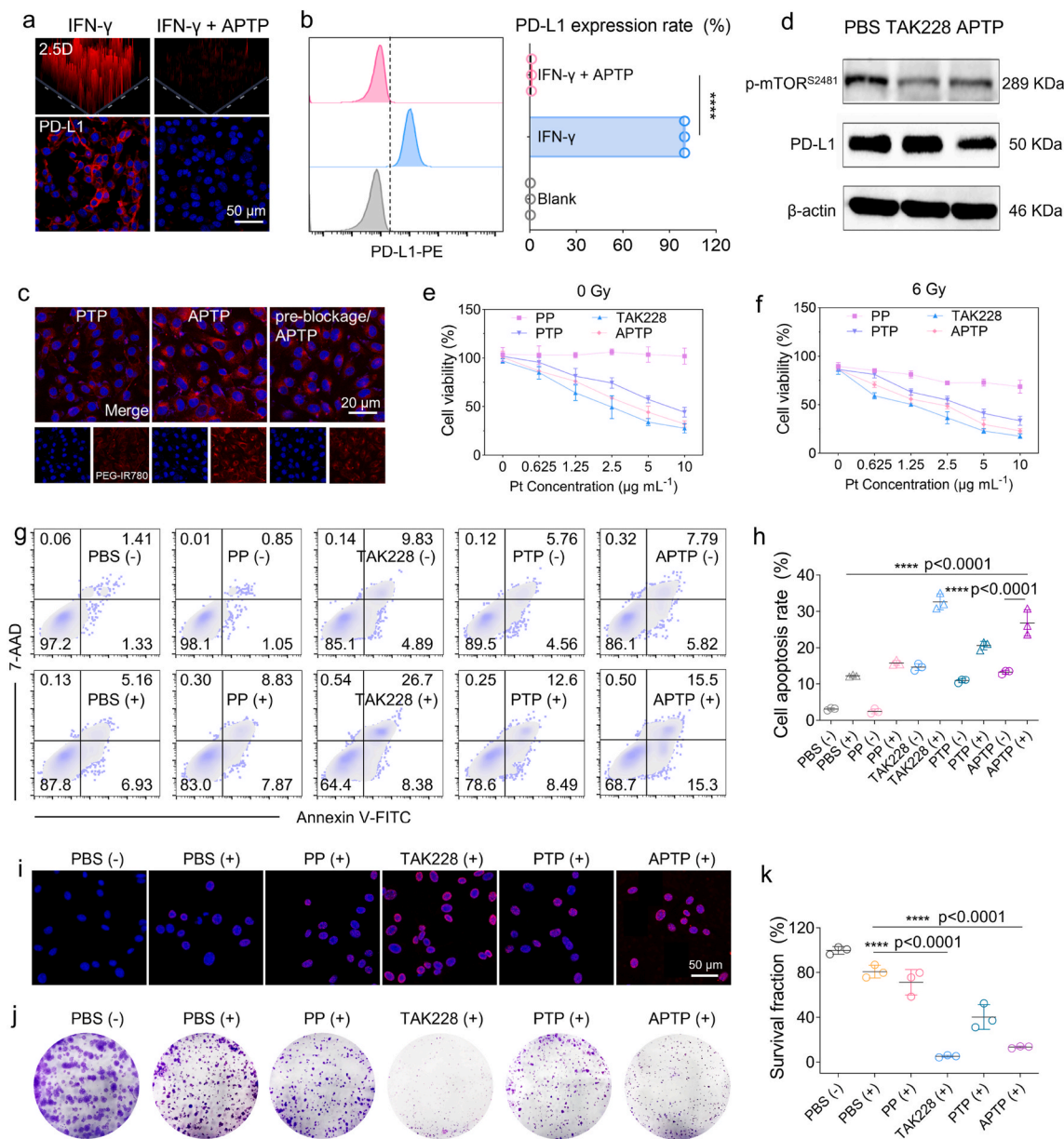


Fig. 3. In vitro evaluation of active targeting and cancer cell inhibition performances of APTP NPs (+). '+' represents X-ray irradiation, '-' represents without X-ray irradiation. **a,b** The CLSM images (a) and FCM analysis (b) of the PD-L1 positive rate of B16F10 cells under the incubation of APTP with the IFN- γ stimulation. **c** Cellular uptake results of different groups, including PTP, APTP, and APTP plus pre-blockage of aPD-L1. **d** The Western blot analysis for PD-L1 and the phosphorylated mTOR under the treatments of TAK228 and APTP NPs. **e,f** Cell viability of B16F10 under the different treatments without (e) or with 6 Gy X-ray irradiation (f). **g,h** Representative flow cytometry plots (g) and quantification analyses (h) of the B16F10 cells' cell apoptosis under the different treatments. **i** Representative DNA damage of B16F10 cells under different treatments. **j,k** Representative clonogenic assay (j) and the corresponding survival fraction (k) of B16F10 cells after different treatments. Data were given as mean \pm S.D. (n = 3). One-way ANOVA analysis with Tukey's multiple comparison test was used. Significance is presented as ****p < 0.0001.

determined. Despite high expression of PD-L1 exhibited in B16F10 cells under IFN- γ stimulation as previously discussed, co-incubation of APTP NPs induced near-total blockade of the PD-L1 ligand, suggesting the active targeting ability of APTP NPs (Fig. 3a). Similarly, the FCM analysis displayed the remarkable PD-L1 blockade effect of APTP NPs (Fig. 3b). To visualize the cell internalization of PTP and APTP, we synthesized PEG-IR780 (the structure was shown in Fig. S8) to blend with amphiphilic PEG-polyphenol, the former endowed nanoparticles with red fluorescence. As shown in Fig. 3c, after the decoration of aPD-L1 on PTP, the internalization into the B16F10 cells was markedly increased compared with PTP NPs. The weaker fluorescence in virtue of the PD-L1 ligand pre-blockage further manifested the aPD-L1-enhanced cell internalization. Theoretically, the aPD-L1-enriched TAK228-loaded nanobroker may block the PD-L1 ligand on the cell membrane pre-emptively, followed by the suppression of cellular mTOR phosphorylation to disable mTOR downstream signal after the cell uptake of APTP NPs [7]. Thereout, the Western blot assay was harnessed to embody the APTP NPs' impact on PD-L1 positive rate and mTOR phosphorylation. As shown in Fig. 3d, the PD-L1 positive rate was remarkably restrained owing to the PD-L1 blockade of APTP NPs. The phosphorylation of mTOR on S2481 (abbreviated as p-mTOR^{S2481}, a mTORC2-selective autophosphorylation site) was lessened under the interference of either TAK228 or APTP NPs. Compared with the impact of TAK228, the intervention to p-mTOR^{S2481} induced by APTP was weaker on account of the latter's moderate drug release. Reasonably, the enhanced cell internalization and mTOR inhibition herald the tumoricidal potential of APTP NPs.

Next, the biocompatibility of PEG-polyphenol and platinum-chelated PEG-polyphenol (denoted as PP) were evaluated preceding the investigation of NPs' in vitro anti-proliferative effects (Fig. S9). The negligible cytotoxicity even at a high concentration (940 $\mu\text{g mL}^{-1}$) revealed the excellent biosafety of PEG-polyphenol and PP. The cell viability of B16F10 cells under the treatment of PP, TAK228, PTP, or APTP NPs with or without X-ray irradiation was assessed by methyl thiazolyl tetrazolium (MTT) assay (Fig. 3e and f), corresponding half inhibitory concentrations (IC50) of each group were exhibited in Table S2. The moderate anti-proliferative effect of PP was observed with the aid of X-ray irradiation (6 Gy), indicating the radiosensitizing effect of the high-Z metal platinum. The TAK228, PTP, and APTP treatments exhibited excellent cytotoxicity, particularly when combined with X-ray irradiation, which might ascribe to the outstanding inhibition of the mTOR signaling pathway. Subsequently, we investigated the underlying anti-tumor mechanisms in quick succession. The proliferative B16F10 cells were arrested in the G1 cycle phase, an intermediate phase preceding DNA replication in mitosis, by the mTOR repression (Fig. S10) [44]. The mTOR repression synchronously elicited desirable cell apoptosis rate, which achieved a substantial augmentation to 30.8% in APTP (+) group compared with other groups (Fig. 3g and h) ('+' represents 'X-ray irradiation', '-' represents 'without X-ray irradiation') [45,46]. Double-stranded DNA break concomitant with the formation of phosphorylated histone H₂AX (γ -H₂AX) incites cell cycle arrest and apoptosis [47,48]. To elucidate the immanent mechanism of APTP NPs' tumoricidal behavior, the γ -H₂AX induced by DNA damage was detected by CLSM (Fig. 3i) [49]. Strong red fluorescence signal observed in the APTP (+) group revealed the apparent DNA damage compared with PBS (+) group. Provenly, the survival fraction of the APTP (+) group in clonogenic assay was decreased to 13% ascribing to the anti-radioresistant function of mTOR inhibitor and the radiosensitizing effect of Pt (Fig. 3j and k). All the results suggested the in vivo tumoricidal potential of APTP NPs under X-ray irradiation.

3.3. In vitro evaluation of the immune-provocative potential of APTP (+)

Considering the tumor-local X-ray irradiation is insufficient to confront arrogant distant or metastatic tumors, the capacity to provoke the tumoricidal immune response becomes a crucial indicator for

evaluating the anti-tumor potential of the customized tactic. As discussed previously, the aPD-L1-enriched nanobroker APTP has the capability of potentiating tumor cell death under X-ray irradiation, which may generate the desirable neoantigen. The tumor-associated antigens (TAAs) are typically captured and reprogrammed by antigen-presenting cells, representatively the dendritic cells (DCs), to promote the activation of T cells (Fig. 4a) [50,51]. Besides, the adsorptive aPD-L1 on APTP can suppress immune escape via interdicting the interaction between tumoral PD-L1 and immune cells' PD-1. Therefore, the APTP NPs may have the ability to provoke the immune response. Here, we co-incubated pretreated B16F10 cells and bone-marrow-derived cells (BMDCs) at a ratio of 1:1 for 24 h and analyzed the maturation of DCs (Fig. 4b–d) [52]. Untreated BMDCs and lipopolysaccharide (LPS)-treated BMDCs were set as negative control and positive control, respectively. Compared with the PBS (+) group, PP (+) treatment subjected DCs maturation to an approximately 9% improvement, indicating the radiosensitization effect of Pt directly. The PTP (+) group exhibited $52.7 \pm 1.4\%$ mature DCs, slightly higher than the $51.9 \pm 1.4\%$ of TAK228 (+) on account of the stress response to nanomaterials [53]. Integrating with TAK228 and aPD-L1 augmented DCs maturation to the percussive level ($58.9 \pm 1.2\%$, in APTP (+) group), which might benefit from aPD-L1/TAK228 cooperative with Pt-enhanced radiotherapy. Mature DCs have been reported to secrete specific proinflammatory cytokines (e. g., interleukin-6 (IL-6), interleukin-12p70 (IL-12p70), and tumor necrosis factor- α (TNF- α)) to orchestrate the tumoricidal immune response [54,55]. Herein, the TNF- α , IL-12p70, and IL-6 in the culture medium supernatant were detected by enzyme-linked immune sorbent assay (ELISA) (Fig. 4e–g). Consistent with DCs maturation, the APTP (+)-treated group exhibited the highest secretion of proinflammatory cytokines. Together, unifying mTOR inhibition, aPD-L1 blockade, and radiosensitization may benefit anti-tumor immune responses.

3.4. Tumor therapeutic performance of APTP (+) in vivo

A highly efficient tumor-selective system can deliver therapeutic cargos into tumors for enhancing anti-tumor efficacy while minimizing adverse effects. As PD-L1 ligand was highly expressed on melanoma cells, we proposed that aPD-L1-decorated nanobroker APTP possessed active tumor targeting ability in virtue of the high binding affinity of PD-L1/aPD-L1 [56]. Here, a unilateral subcutaneous B16F10 tumor-bearing mouse model was utilized to explore the tumor accumulation via an in vivo fluorescence imaging system (IVFIS). Similar to cell internalization assay, the PEG-IR780 was adopted to blend with PEG-polyphenol to fabricate fluorescent nanobroker for tracking accumulation. The fluorescence images and quantitative analysis results in Fig. S11 revealed that both IR780-fabricated PTP and APTP NPs accumulated within tumor region gradually and reached the plateau at 12 h post intravenous (i.v.) injection, while the tumor accumulation efficacy of APTP NPs benefiting from the adsorption of aPD-L1 was obviously stronger than PTP NPs. Moreover, the comparatively greater tumor accumulation efficiency and longer retention time of APTP NPs in contrast with PTP NPs indicated the preeminent tumor targeting and durable tumor killing capabilities of APTP nanobroker.

Subsequently, a bilateral subcutaneous B16F10 tumor-bearing C57BL/6J female mouse model was established to examine tumoricidal effect of APTP NPs (Fig. 5a). The X-ray irradiation was performed in the left flank tumor (primary tumor) at the 12-h point post i.v. administration when the tumor volume reached circa 150 mm³. The treatment loop was executed three consecutive times, concomitant with the monitoring of tumor volume and body weight every other day. All treated mice were euthanized to harvest tumors, major organs, and sera for further analyses on the tenth day. Compared with barely restrained primary tumor growth in the PBS (+) group, moderate tumor inhibition occurred in the PP (+) group owing to Pt-mediated radiosensitizing effect (Fig. 5b and Fig. S12). Additionally, arming the radiosensitizing function of Pt with an anti-tumorigenic mTOR inhibitor hoisted the

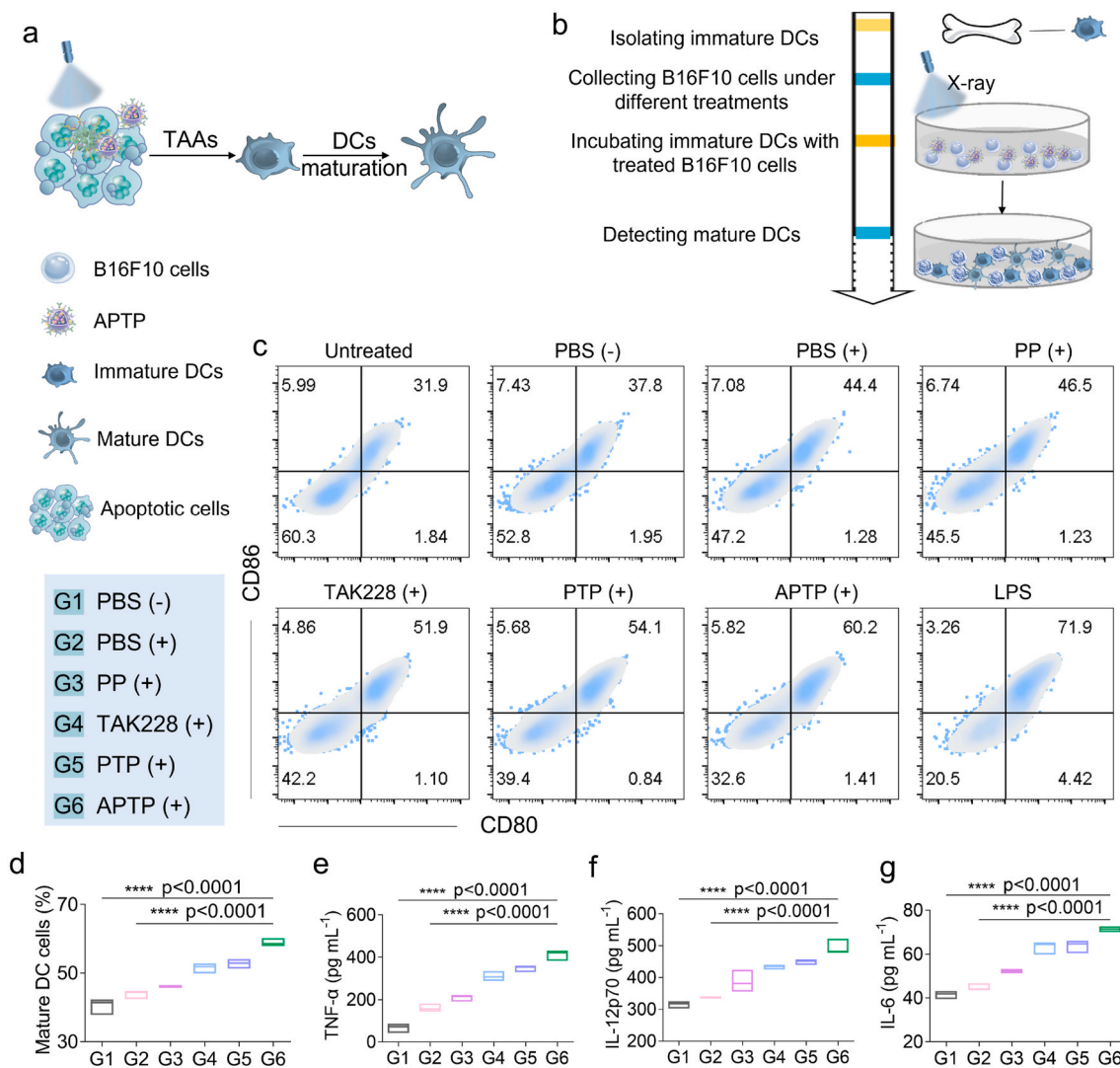


Fig. 4. In vitro evaluation of the immune-provocative potential of APTP NPs. ‘+’ represents X-ray irradiation, ‘-’ represents without X-ray irradiation. **a** Illustration of the TAAs-stimulated DCs maturation. **b** Schematic illustration of the BMDCs maturation detection in vitro. **c,d** FCM plots and quantitative analysis of mature DCs (CD11c⁺CD80⁺CD86⁺) under the different treatments in a co-incubation system for 24 h. **e-g** ELISA detection results of proinflammatory cytokines (TNF-α, IL-12p70, and IL-6) in the supernatant medium after the 24 h co-incubation. Data are presented as mean ± SD (n = 3). One-way ANOVA analysis with Tukey’s multiple comparison test was used. Significance is presented as ****p < 0.0001.

radiotherapeutic efficacy (G5). Further, integrating aPD-L1 and mTOR inhibitor with Pt-enhanced radiotherapy drove the tumor elimination more prominently (G6), attributed to the dual brake of melanoma-intrinsic tumorigenesis signal, including PD-L1 ligand blockade and mTOR inhibition. Intriguingly, in contrast to the best anti-proliferative effect of mTOR inhibitor TAK228 plus X-ray irradiation in vitro, its anti-tumor therapeutic effect (G4) in vivo was apparently weaker than that of APTP (+) group (G6). The prominent tumor-targeting performance and aPD-L1-mediated interdiction (melanoma-PD-L1: melanoma-PD-1 interaction and melanoma-PD-L1:lymphocyte-PD-1 interaction) of the aPD-L1-enriched nanobroker APTP NPs might be responsible for that phenomenon. A similar trend was observed in distant tumors (Fig. 5c and Fig. S13). Compared with other groups, the APTP (+) group displayed superior distant tumor inhibition. Furthermore, the hematoxylin and eosin (H&E) staining of bilateral tumors confirmed the extensive tumor damage (comparative undertint region represents the cells without the nucleus) induced by the nanobroker APTP plus X-ray irradiation, while modest apoptosis occurred in the TAK228 (+) and PTP (+) group (Fig. 5d) [57]. Besides, the biosafety of the nanobroker APTP NPs was attested by the negligible body weights

variation and no significant difference in serum biochemistry (Fig. 5e and Fig. S14). The typical biomarkers for serum biochemistry analysis included blood urea nitrogen (BUN), creatine kinase (CK), creatinine (CRE), aspartate transaminase (AST), and alanine aminotransferase (ALT).

Ultimately, we explored the survival rate in a subcutaneous B16F10 tumor-bearing mouse model to validate the survival benefits of the nanobroker (Fig. 5f). The treatment procedure was consistent with the tumor therapeutic experiment, concomitant with the tumor volume monitoring every four days. All treated mice were euthanized once the tumor volume exceeded the stipulation (2000 mm³). Sixty percent of mice underlying APTP (+) treatment survived over 42 days, evidently longer than other treated groups (Fig. 5g). The long-term tumor volume variations of different groups were exhibited in Fig. 5h to highlight the survival prolongation performance of our nanobroker. Collectively, the eminent tumoricidal effect and survival prolongation performance of our nanobroker APTP NPs with reliable biosafety suggested the expectable biomedical applications.

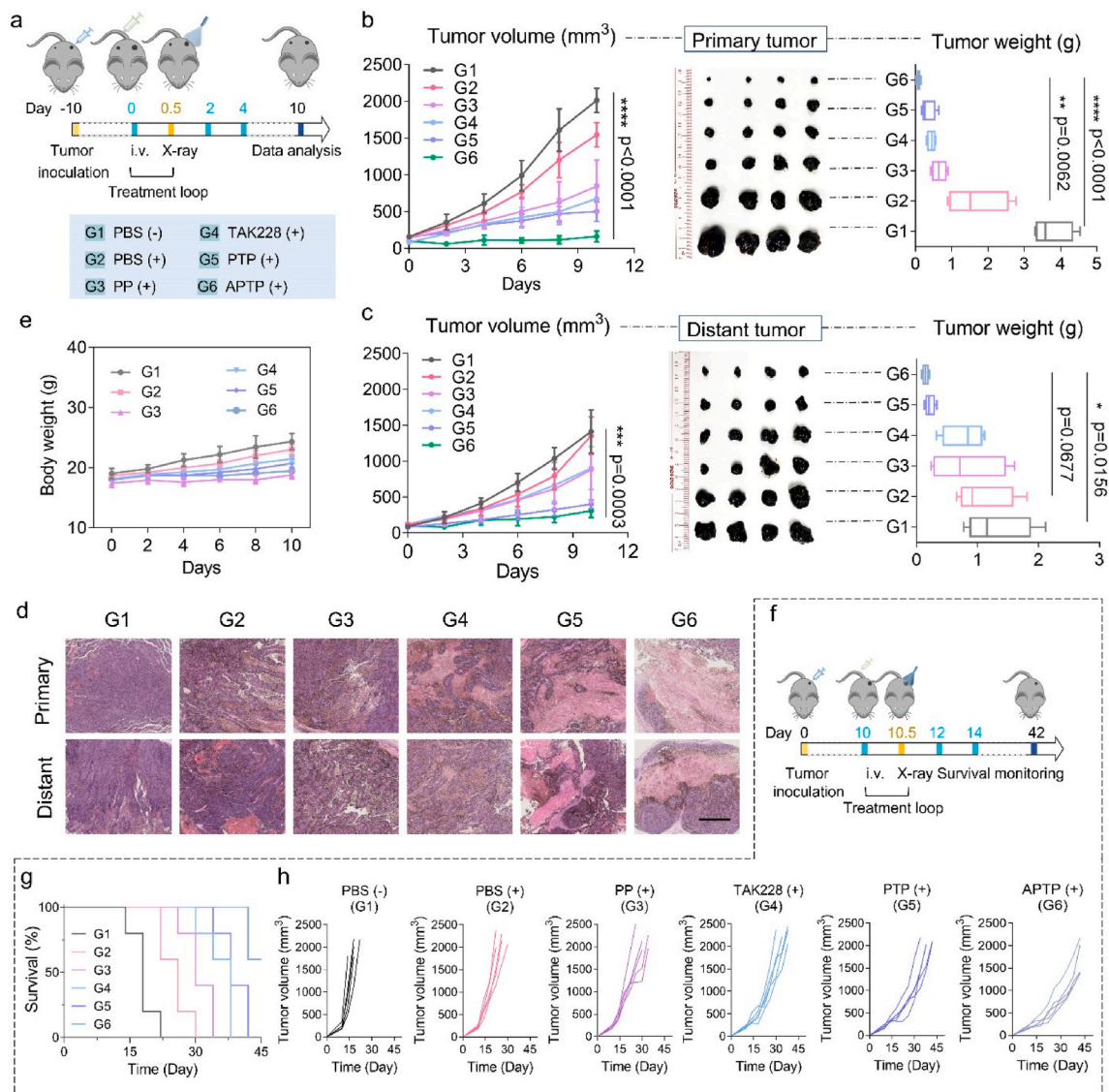


Fig. 5. Tumoricidal effect and survival prolongation behavior of APTP NPs in vivo. ‘+’ represents X-ray irradiation, ‘-’ represents without X-ray irradiation. **a** Schematic illustration of tumor therapeutic procedure in vivo. **b,c** Tumor volume and weight variation curves of the primary (**b**) and distant tumors (**c**) under various treatments. **d** H&E staining of the primary and distant tumors under various treatments. Scale bar = 500 μ m **e** Body weight variation of mice treated by different methods. **f** Schematic illustration of experiment procedure to assess the survival rate under various treatments in vivo. **g** Survival rates under the different treatments. **h** Tumor growth curves of different groups. Data are presented as mean \pm SD ($n = 4$ in **b,c,e**, and $n = 5$ in **g,h**). One-way ANOVA analysis with Tukey’s multiple comparison test was used. Significance is presented as * $p < 0.05$, ** $p < 0.01$, *** $p < 0.001$, and **** $p < 0.0001$.

3.5. Tumoricidal mechanism of APTP (+)

To gain a rough insight into the mechanism of the outstanding tumoricidal effects of APTP plus X-ray irradiation, we performed the quantitative proteomics analysis of the tumors. Tandem mass tags based on the quantitative proteomics profiling techniques successfully identified 5556 distinct proteins. Among which, 618 proteins were considered as differential proteins (Fold change ≥ 2 or ≤ 0.5 , $P < 0.05$) in APTP (+)-treated tumors compared with PBS (-)-treated tumors, signifying the cogent regulation effect to the intracellular signaling pathway by APTP (+) (Fig. 6a and Fig. S15) [58]. Further, the Encyclopedia of Genes and Genomes (KEGG) database was utilized to assign the functional genome products involved in the nanobreaker’s treatment to sort specific biological pathways out (Fig. 6b and Fig. S16). We excitedly found that considerable leverage of our nanobreaker was embodied in the regulation of multiple metabolic pathways, representatively the galactose metabolism, the glycolysis gluconeogenesis, and the glycine, serine and threonine metabolism. Considering that mTOR kinase is the

predominant coordinator for commanding cancer metabolism [6,59,60], mTOR inhibitor TAK228 loaded in the nanobreaker might be responsible for the prominent metabolic regulation that transpired in the KEGG analysis. Significant differences in apoptosis and lysosome pathways were traced down in the KEGG analysis as well, unveiling the predominant tumor death pathways provoked by APTP (+). Of note, HIF-1 α /VEGF signaling pathway under the APTP (+) treatment exhibited significant differences compared with the control group. Mechanistically, restraining mTOR signaling might suppress the expression of cMYC and HIF-1 α to thwart tumorigenesis and angiogenesis (Fig. 6c) [61,62]. The KEGG analysis related to HIF-1 α /VEGF pathway regulation suggested the sabotage of tumor mTOR signal mediated by our nanobreaker APTP encapsulated dual mTORC1/2 inhibitor TAK228.

To elaborate on the concrete mechanisms involved in the tumor killing and survival prolongation, we originate a deeper investigation of fractional tumors harvested in the therapeutic experiment in virtue of Western blot assay (Fig. 6d). Here, PBS (+) group was preferred as the

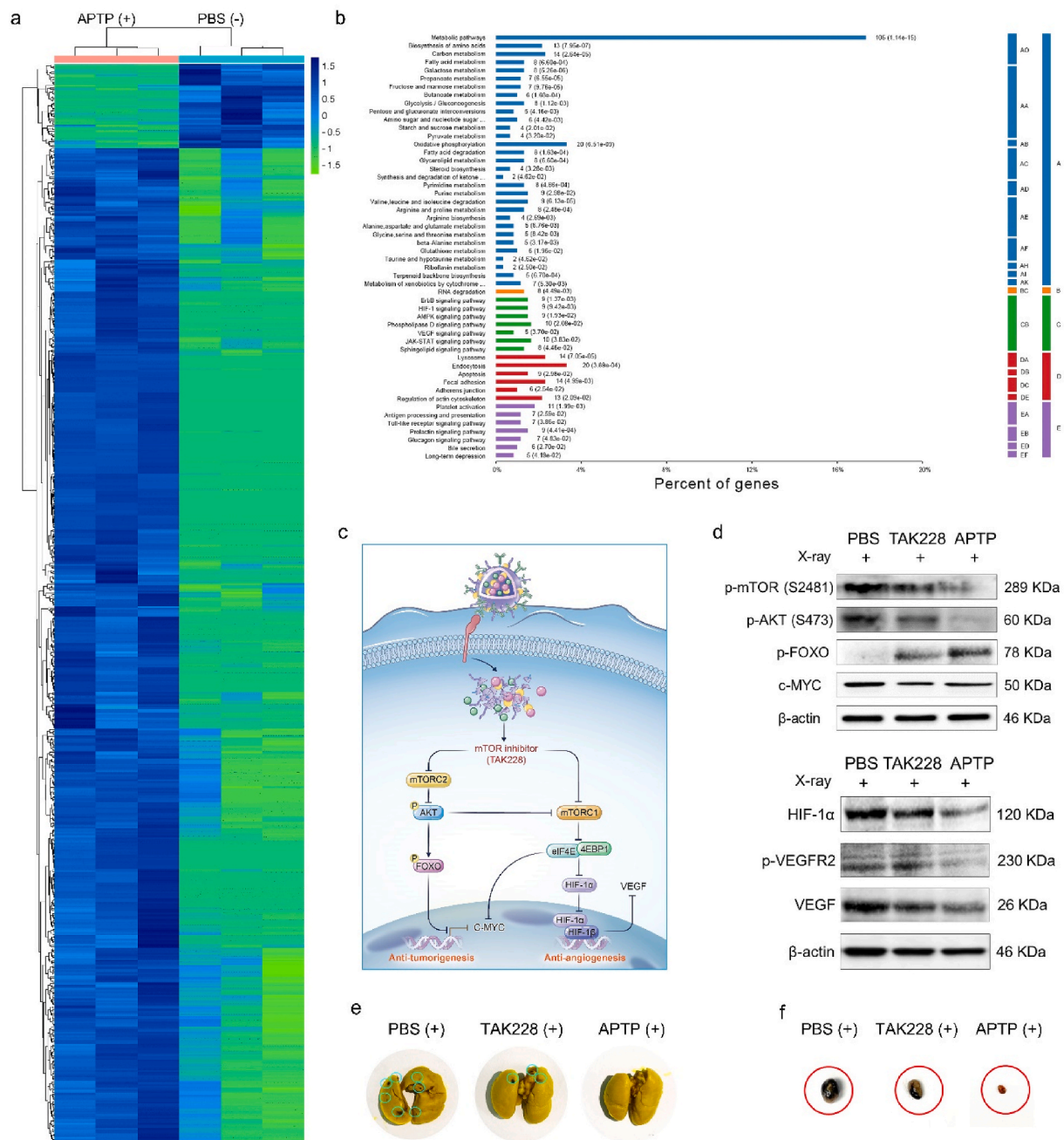


Fig. 6. The potential tumoricidal mechanism of APTP (+) in vivo. ‘+’ represents X-ray irradiation, ‘-’ represents without X-ray irradiation. **a** Heat map of the significant proteins’ variation under the treatment of APTP (+). **b** Proteomics KEGG enrichment analysis on markedly varied genome products after the treatment of APTP (+). **c** The potential regulatory mechanism of mTOR downstream signaling pathway. **d** Western blot analysis of the mTOR/cMYC axis and mTORC1/HIF-1 α /VEGF axis treated by PBS (+), TAK228 (+), and APTP (+). **e** Photographs of melanoma lung metastasis of PBS (+), TAK228 (+), and APTP (+) groups. **f** Photographs of melanoma lymphatic metastasis of PBS (+), TAK228 (+), and APTP (+) groups.

negative control to decrease the parameter variable. The key proteins in the mTOR signaling pathway, including p-mTOR^{S2481}, p-AKT^{S473}, p-FOXO1^{S256}, and cMYC in the mTOR/cMYC axis, and HIF-1 α , p-VEGFR2, and VEGF in the mTORC1/HIF-1 α /VEGF axis were detected. β -actin was used as the internal standard protein. Compared with the PBS (+) group, the expression of proteins correlated with the mTOR/cMYC and mTORC1/HIF-1 α /VEGF signaling pathways was downregulated except for the p-FOXO1^{S256} within the interference of either TAK228 (+) or APTP NPs (+) (Fig. 6d). Moreover, APTP (+) displayed a higher intervention efficacy of protein expression than the TAK228 (+), which may be ascribed to the considerable tumoral accumulation of APTP NPs. In accordance with the downregulation of HIF-1 α /VEGF axis, the

weakened histological immunofluorescence of platelet endothelial cell (staining CD31 marker) reconfirmed that both TAK228 (+) and APTP NPs (+) crippled angiogenesis compared with PBS (+) (Fig. S17). On account of the angiogenesis is closely relevant with tumor metastasis, we reasonably speculated that the downregulation of HIF-1 α might be conducive to anti-metastasis [17,63]. Lungs and tumor-draining lymph nodes (TDLNs) were harvested to assess the melanoma metastasis. Compared with the PBS (+) group, the pulmonary metastatic nodules displayed a notable reduction in the TAK228 (+) group (Fig. 6e and Fig. S18). Most notably, lung metastasis seemed to be entirely repressed after APTP (+) treatment. The lymphatic metastasis of different groups was consistent with the lung metastasis (Fig. 6f), indicating the

substantial anti-metastatic benefits of our nanobroker APTP NPs via downregulating the HIF-1 α signaling. Conclusively, the repression of metabolic and growth signals (mainly focused on oncogenic cMYC and pro-angiogenic HIF-1 α) might be the mainspring of our nanobroker's eminent tumoricidal effect and survival prolongation.

Furthermore, the proteins correlated with platelet activation, toll-like receptor signaling pathway, and antigen processing and presentation were traced down in the KEGG analysis after APTP (+) treatment, indicating the amassment of adaptive immune surveillance (Fig. 6b) [64,65]. The immune-related signaling pathways enriched by KEGG guided us to further explore the immanently tumoricidal mechanism.

3.6. Immunological effect invoked by APTP (+)

To assess the immunological effect of APTP (+), we retrieved tumor-draining lymph nodes, spleens, and tumors of the mice underlying treatments and dissociated them into single-cell suspensions for flow cytometric analysis (Fig. 7a). Since antigen processing and presentation mediated by antigen-presenting cells are indispensable for awakening

adaptive immune response, we first examined the proportion of mature DCs in TDLNs (Fig. 7b and c). The mice receiving PBS (+) treatment presented a higher DCs maturation rate ($39.8 \pm 3.9\%$) in comparison with the mice receiving PBS (-) treatment ($30.1 \pm 6.3\%$), demonstrating that radiotherapy was beneficial for the immune activation. Owing to the radiosensitization effect of platinum and anti-radioreistance of mTOR inhibitor TAK228, the DCs maturation rate of the PP (+) group ($46.95 \pm 6.7\%$) and TAK228 (+) group ($49.3 \pm 5.7\%$) were apparently augmented. Significantly, a further increase ($53.3 \pm 3.1\%$ in the APTP (+) group) was observed when integrating the platinum and mTOR inhibitor with aPD-L1 antibody. The highest DCs maturation rate of the APTP (+) group predicted the potential immunostimulation induced by our nanobroker APTP NPs consolidated with radiotherapy. Subsequently, the proliferation marker Ki67 and activation marker Granzyme B (GzmB) were detected to evaluate the CD8⁺ T cell activation in TDLNs (Fig. 7d and e and Figs. S19 and S20). Consistent with the DCs maturation, the APTP (+) treatment engaged the highest CD8⁺ T cell activation (embodied in Ki67⁺ CD8⁺ T cells and GzmB⁺ CD8⁺ T cells) in TDLNs contrasted with other treatments.

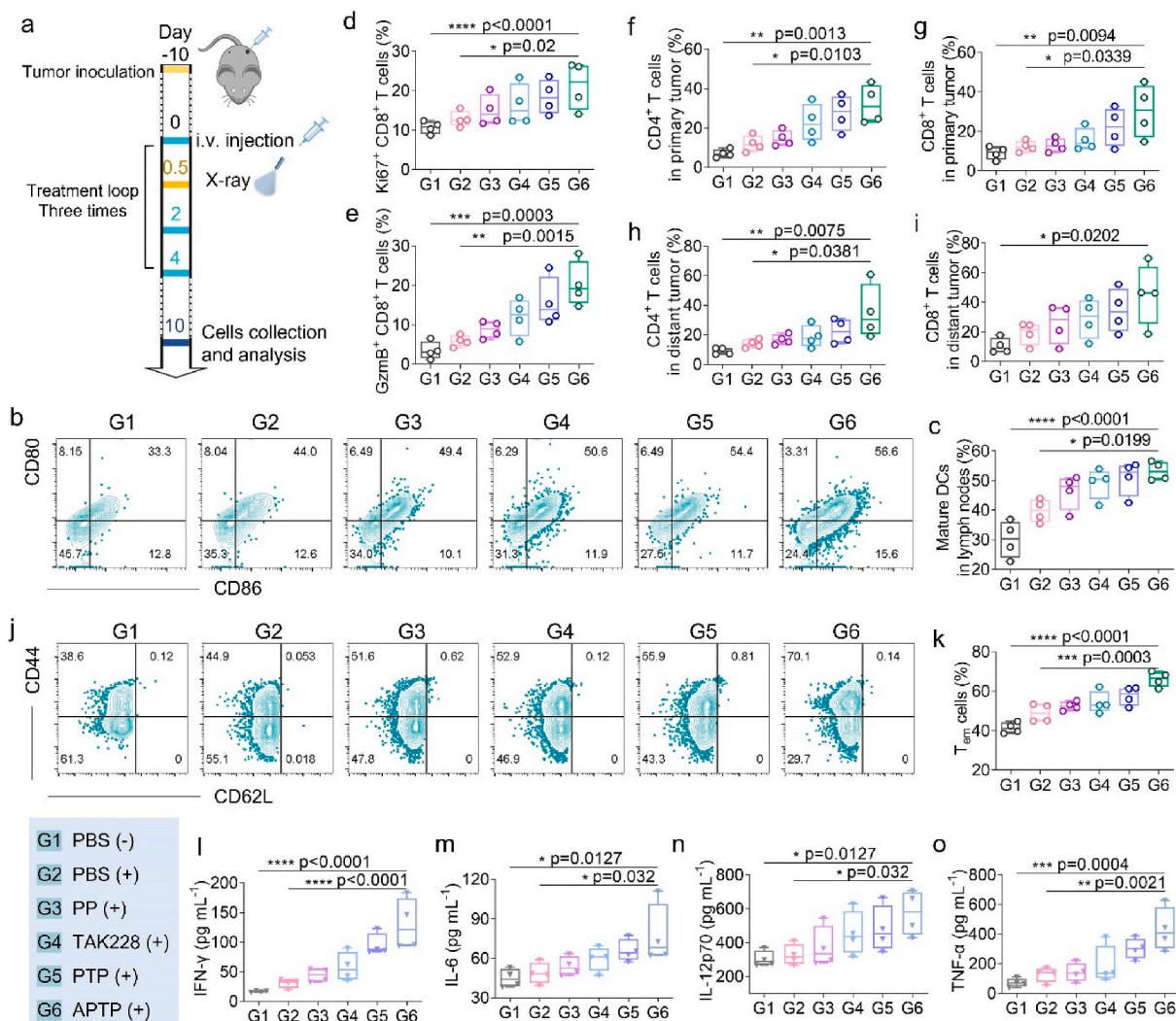


Fig. 7. Immunological effect provoked by APTP NPs plus X-ray irradiation. '+' represents with X-ray irradiation, '-' represents without X-ray irradiation. **a** Schematic illustration of tumor therapeutic procedure in vivo. **b,c** Representative flow cytometry plots (**b**) and quantitative analysis results of lymphatic derived DCs maturation (CD11c⁺CD80⁺CD86⁺, gated on CD11c⁺ DCs) under different treatments. **d,e** Quantitative analysis of Ki67⁺ (**d**) and GzmB⁺ (**e**) CD8⁺ T cells in lymph nodes after gating on CD3⁺CD8⁺ T cells under different treatments. **f-i** CD8⁺ and CD4⁺ T cells after gating on CD45⁺CD3⁺ T cells in primary and distant tumors. **j,k** Representative flow cytometry plots (**j**) and quantitative analysis (**k**) of effector memory T cells (CD3⁺CD8⁺CD44⁺CD62L⁻, gated on CD3⁺CD8⁺ T cells) in spleens under different treatments. **l-o** IFN- γ , IL-6, IL-12p70, and TNF- α secretion in serum under different treatments. Data are presented as mean \pm SD (n = 4). One-way ANOVA analysis with Tukey's multiple comparison test was used. Significance is presented as *p < 0.05, **p < 0.01, ***p < 0.001, and ****p < 0.0001.

Excitedly, the tumor-infiltrating T lymphocytes within primary and distant tumors earned similar variation trend. The highest proportion of tumor-infiltrating CD4⁺ T cells (approximately 29.5% in primary tumors; 35.3% in distant tumors) and CD8⁺ T cells (approximately 30.3% in primary tumors; 47.8% in distant tumors) occurred in the APTP (+) group (Fig. 7f–i and Figs. S21–24), substantiating the splendid immunostimulatory capability of APTP (+).

To analyze the long-term tumor depression capacity engendered by our nanobroker cooperated with radiotherapy, we detected the proportion of splenic effector memory T cells (T_{em} cells, CD3⁺CD8⁺CD44⁺CD62L⁻ gated on CD8⁺ T cells) in all treated spleens (Fig. 7j and k). In comparison to the PBS (–) group (41.4 ± 2.7%), a slight increase in the percentage of T_{em} cells was exhibited after PP (+) (53.2 ± 2.9%) or TAK228 (+) (54.2 ± 5.7%) treatments. Notably, orchestrating platinum, mTOR inhibitor TAK228, and anti-PD-L1 antibody with X-ray irradiation substantially invigorated the expansion of T_{em} cells, as the 66.1 ± 3.9% in the APTP (+) group. The variation of T_{em} cells was in accordance with other immunological results. Moreover, the pro-inflammatory cytokines (IFN-γ, IL-6, IL-12p70, and TNF-α) in all treated serum were detected via ELISA kits. The highest concentration of these cytokines in the APTP (+) group reconfirmed the optimal immunoprovoking effect of our nanobroker in comparison to other groups (Fig. 7l–o and Fig. S25). Conclusively, the three-pronged nanobroker plus X-ray irradiation elicited robust antitumor immunity and long-term immunological memory.

4. Conclusion

Melanoma-cell intrinsic PD-1: PD-L1 interaction accelerates the tumorigenesis, angiogenesis, and radioresistance via hyperactivating mTOR signaling pathway. Hence, we orchestrated high-Z platinum, TAK228 (mTOR inhibitor) with aPD-L1 to form a three-pronged nanobroker for thwarting melanoma cell-intrinsic protumorigenic and proangiogenic signaling and sensitizing radiotherapy to accelerate tumor death. In this nanobroker, TAK228 and aPD-L1 were federatively harnessed to interdict melanoma intrinsic PD-1:PD-L1 protumorigenic and proangiogenic signaling by blocking PD-1-driven mTOR signaling and melanoma-PD-L1 ligand. Specifically, the inhibition of mTOR signaling was conducive to downregulating mTOR downstream protumorigenic cMYC and proangiogenic HIF-1α, which ultimately cripple tumor growth and metastasis. Moreover, the anti-radioresistant TAK228 contributed to Pt-sensitized radiotherapy, which was conducive to the tumor repression and the awakening of tumoricidal immune response. The blockade of melanoma-PD-L1 ligand was beneficial for invigorating cytotoxicity T cells infiltration concurrently. Hereto, this three-pronged platinum@polymer-catechol nanobroker plus X-ray irradiation faded melanoma aggression away and prolonged the mice survival rate in the subcutaneous B16F10 tumor-bearing mouse model. The tactful hindrance of melanoma protumorigenic signaling mediated by our nanobroker might endow melanoma-bearing patients with substantial benefits in the clinic.

CRedit authorship contribution statement

Wenxi Li: Writing – original draft, conceived and designed the research, prepared the nanobroker, determined the characters, and performed the cell experiments, performed the animal experiments, wrote the paper. **Jie Yan:** Writing – original draft, prepared the nanobroker, determined the characters, and performed the cell experiments, performed the animal experiments, wrote the paper. **Hao Tian:** synthesized the PEG-polyphenol. **Bei Li:** Writing – original draft, wrote the paper. **Guohao Wang:** performed the animal experiments. **Wei Sang:** performed the animal experiments. **Zhan Zhang:** performed the animal experiments. **Xuanjun Zhang:** wrote the paper, Writing – original draft. **Yunlu Dai:** Writing – original draft, conceived and designed the research, wrote the paper.

Declaration of competing interest

The authors declare that they have no known competing financial interests or personal relationships that could have appeared to influence the work reported in this paper.

Acknowledgements

This work was supported by the National Natural Science Foundation of China (NSFC 32171318 and 32101069), the Faculty of Health Sciences, University of Macau, the Science and Technology Development Fund, Macau SAR (File no. 0109/2018/A3, 0011/2019/AKP, 0113/2019/A2, 0103/2021/A, and 0002/2021/AKP), the Multi-Year Research Grant (MYRG) of University of Macau (File no. MYRG2022-00011-FHS) and Shenzhen Science and Technology Innovation Commission, Shenzhen-Hong Kong-Macau Science and Technology Plan C (No. SGDX20201103093600004). We appreciate the assistance and support from the Proteomics, Metabolomics and Drug Development Core, Animal Research Core, and Biological Imaging and Stem Cell Core in the Faculty of Health Sciences, University of Macau.

Appendix A. Supplementary data

Supplementary data to this article can be found online at <https://doi.org/10.1016/j.bioactmat.2022.09.006>.

References

- [1] M. Bittner, P. Meltzer, Y. Chen, et al., Molecular classification of cutaneous malignant melanoma by gene expression profiling, *Nature* 406 (6795) (2000) 536–540.
- [2] D. Schadendorf, D.E. Fisher, C. Garbe, et al., Melanoma, *Nat. Rev. Dis. Primers* 1 (2015), 15003.
- [3] M. Streit, M. Detmar, Angiogenesis, lymphangiogenesis, and melanoma metastasis, *Oncogene* 22 (20) (2003) 3172–3179.
- [4] M.B. Faries, J.F. Thompson, A.J. Cochran, et al., Completion dissection or observation for sentinel-node metastasis in melanoma, *N. Engl. J. Med.* 376 (23) (2017) 2211–2222.
- [5] S. Kleffel, C. Posch, S.R. Barthel, et al., Melanoma cell-intrinsic PD-1 receptor functions promote tumor growth, *Cell* 162 (6) (2015) 1242–1256.
- [6] R.A. Saxton, D.M. Sabatini, Mtor signaling in growth, metabolism, and disease, *Cell* 168 (6) (2017) 960–976.
- [7] A.C. Hsieh, Y. Liu, M.P. Edlind, et al., The translational landscape of mTOR signalling steers cancer initiation and metastasis, *Nature* 485 (7396) (2012) 55–61.
- [8] K.M. Dodd, J. Yang, M.H. Shen, J.R. Sampson, A.R. Tee, Mtorc1 drives hif-1alpha and vegf-a signalling via multiple mechanisms involving 4e-bp1, s6k1 and stat3, *Oncogene* 34 (17) (2015) 2239–2250.
- [9] Z.E. Stine, Z.E. Walton, B.J. Altman, A.L. Hsieh, C.V. Dang, Myc, metabolism, and cancer, *Cancer Discov.* 5 (10) (2015) 1024–1039.
- [10] K. Masui, K. Tanaka, D. Akhavan, et al., Mtor complex 2 controls glycolytic metabolism in glioblastoma through foxo acetylation and upregulation of c-myc, *Cell Metabol.* 18 (5) (2013) 726–739.
- [11] S. Matkar, P. Sharma, S. Gao, B. Gurung, B.W. Katona, J. Liao, A.B. Muhammad, X.-C. Kong, L. Wang, G.J. Jin, An epigenetic pathway regulates sensitivity of breast cancer cells to her2 inhibition via foxo/c-myc axis, *Cancer Cell* 28 (4) (2015) 472–485.
- [12] D. Silvera, S.C. Formenti, R.J. Schneider, Translational control in cancer, *Nat. Rev. Cancer* 10 (4) (2010) 254–266.
- [13] D.-H. Kim, D.D. Sarbassov, S.M. Ali, J.E. King, R.R. Latek, H. Erdjument-Bromage, P. Tempst, D.M. Sabatini, Mtor interacts with raptor to form a nutrient-sensitive complex that signals to the cell growth machinery, *Cell* 110 (2) (2002) 163–175.
- [14] X.M. Ma, J. Blenis, Molecular mechanisms of mtor-mediated translational control, *Nat. Rev. Mol. Cell Biol.* 10 (5) (2009) 307–318.
- [15] A.Y. Choo, S.-O. Yoon, S.G. Kim, P.P. Roux, J. Blenis, Rapamycin differentially inhibits s6ks and 4e-bp1 to mediate cell-type-specific repression of mrna translation, *Proc. Natl. Acad. Sci. USA* 105 (45) (2008) 17414–17419.
- [16] A. Castell, L.G. Larsson, Targeting myc translation in colorectal cancer, *Cancer Discov.* 5 (7) (2015) 701–703.
- [17] W.G. Kaelin Jr., P.J. Ratcliffe, Oxygen sensing by metazoans: the central role of the hif hydroxylase pathway, *Mol. Cell.* 30 (4) (2008) 393–402.
- [18] C.C. Hudson, M. Liu, G.G. Chiang, D.M. Otterness, D.C. Loomis, F. Kaper, A. J. Giaccia, R.T. Abraham, Regulation of hypoxia-inducible factor 1alpha expression and function by the mammalian target of rapamycin, *Mol. Cell Biol.* 22 (20) (2002) 7004–7014.
- [19] J. Lee, A.A. Abdeen, J. Hedhli, K.L. Wycislo, I.T. Dobrucki, T.M. Fan, L. W. Dobrucki, K.A. Kilian, Melanoma topology reveals a stem-like phenotype that promotes angiogenesis, *Sci. Adv.* 3 (10) (2017), e1701350.

- [20] Y. Guri, M.N. Hall, Mtor signaling confers resistance to targeted cancer drugs, *Trends Cancer* 2 (11) (2016) 688–697.
- [21] L. Chang, P.H. Graham, J. Ni, J. Hao, J. Buccu, P.J. Cozzi, Y. Li, Targeting pi3k/akt/mtor signaling pathway in the treatment of prostate cancer radioresistance, *Crit. Rev. Oncol. Hematol.* 96 (3) (2015) 507–517.
- [22] L. Fu, X. Ma, Y. Liu, Z. Xu, Z. Sun, Applying nanotechnology to boost cancer immunotherapy by promoting immunogenic cell death, *Chin. Chem. Lett.* 33 (4) (2022) 1718–1728.
- [23] W. Zhang, F. Wang, C. Hu, Y. Zhou, H. Gao, J. Hu, The progress and perspective of nanoparticle-enabled tumor metastasis treatment, *Acta Pharm. Sin. B.* 10 (11) (2020) 2037–2053.
- [24] L. Zhang, L.T. Røling, X. Wang, et al., Platinum-based nanocages with subnanometer-thick walls and well-defined, controllable facets, *Science* 349 (6246) (2015) 412–416.
- [25] Z. Zhang, L. Xie, Y. Ju, Y. Dai, Recent advances in metal-phenolic networks for cancer theranostics, *Small* 17 (43) (2021), e2100314.
- [26] H. Geng, Q.Z. Zhong, J. Li, Z. Lin, J. Cui, F. Caruso, J. Hao, Metal ion-directed functional Metal–Phenolic materials, *Chem. Rev.* 122 (13) (2022) 11432–11473.
- [27] J. Guo, Y. Ping, H. Ejima, et al., Engineering multifunctional capsules through the assembly of metal-phenolic networks, *Angew. Chem. Int. Ed.* 53 (22) (2014) 5546–5551.
- [28] S. Pan, E. Goudeli, J. Chen, Z. Lin, Q.Z. Zhong, W. Zhang, H. Yu, R. Guo, J. Richardson, F. Caruso, Exploiting supramolecular dynamics in metal-phenolic networks to generate metal-oxide and metal-carbon networks, *Angew. Chem. Int. Ed.* 60 (26) (2021) 14586–14594.
- [29] Z. Ren, S. Sun, R. Sun, G. Cui, L. Hong, B. Rao, A. Li, Z. Yu, Q. Kan, Z. Mao, A metal-polyphenol-coordinated nanomedicine for synergistic cascade cancer chemotherapy and chemodynamic therapy, *Adv. Mater.* 32 (6) (2020), e1906024.
- [30] G. Song, L. Cheng, Y. Chao, K. Yang, Z. Liu, Emerging nanotechnology and advanced materials for cancer radiation therapy, *Adv. Mater.* 29 (32) (2017), 1700996.
- [31] Y. Li, K.H. Yun, H. Lee, S.H. Goh, Y.G. Suh, Y. Choi, Porous platinum nanoparticles as a high-z and oxygen generating nanozyme for enhanced radiotherapy in vivo, *Biomaterials* 197 (2019) 12–19.
- [32] D. Salado-Leza, E. Porcel, X. Yang, L. Stefancikova, M. Bolsa-Ferruz, F. Savina, D. Drago, J.L. Guerin-Kern, T.D. Wu, R. Hirayama, H. Remita, S. Lacombe, Green one-step synthesis of medical nanoagents for advanced radiation therapy, *Nanotechnol. Sci. Appl.* 13 (2020) 61–76.
- [33] T. Bian, A. Gardin, J. Gemen, L. Houben, C. Perego, B. Lee, N. Elad, Z. Chu, G. M. Pavan, R. Klajn, Electrostatic co-assembly of nanoparticles with oppositely charged small molecules into static and dynamic superstructures, *Nat. Chem.* 13 (10) (2021) 940–949.
- [34] W. Zhang, Q.A. Besford, A.J. Christofferson, P. Charchar, J.J. Richardson, A. Elbourne, K. Kempe, C.E. Hagemeyer, M.R. Field, C.F. McConville, I. Yarovsky, F. Caruso, Cobalt-directed assembly of antibodies onto metal-phenolic networks for enhanced particle targeting, *Nano Lett.* 20 (4) (2020) 2660–2666.
- [35] C. Lhuillier, N.P. Rudqvist, T. Yamazaki, Z. Zhang, M. Charpentier, L. Galluzzi, N. Dephore, C.C. Clement, L. Santambrogio, X.K. Zhou, S.C. Formenti, S. Demaria, Radiotherapy-exposed cd8+ and cd4+ neoantigens enhance tumor control, *J. Clin. Invest.* 131 (5) (2021), e138740.
- [36] M. McLaughlin, E.C. Patin, M. Pedersen, A. Wilkins, M.T. Dillon, A.A. Melcher, K. J. Harrington, Inflammatory microenvironment remodelling by tumour cells after radiotherapy, *Nat. Rev. Cancer* 20 (4) (2020) 203–217.
- [37] G. Toda, T. Yamauchi, T. Kadowaki, K.J.S.p. Ueki, Preparation and culture of bone marrow-derived macrophages from mice for functional analysis, *STAR Protoc.* 2 (1) (2021), 100246.
- [38] K. Inaba, M. Inaba, N. Romani, H. Aya, M. Deguchi, S. Ikehara, S. Muramatsu, R. M. Steinman, Generation of large numbers of dendritic cells from mouse bone marrow cultures supplemented with granulocyte/macrophage colony-stimulating factor, *J. Exp. Med.* 176 (6) (1992) 1693–1702.
- [39] A. Garcia-Diaz, D.S. Shin, B.H. Moreno, J. Saco, H. Escuin-Ordinas, G.A. Rodriguez, J.M. Zaretsky, L. Sun, W. Hugo, X. Wang, G. Parisi, C.P. Saus, D.Y. Torrejon, T. G. Graeber, B. Comin-Anduix, S. Hu-Lieskovan, R. Dainoff, R.S. Lo, A. Ribas, Interferon receptor signaling pathways regulating pd-1 and pd-12 expression, *Cell Rep.* 19 (6) (2017) 1189–1201.
- [40] D. Wu, J. Zhou, M.N. Creyer, W. Yim, Z. Chen, P.B. Messersmith, J.V. Jokerst, Phenolic-enabled nanotechnology: versatile particle engineering for biomedicine, *Chem. Soc. Rev.* 50 (2021) 4432–4483.
- [41] W. Horsley, H. Sternlicht, Carbon-13 magnetic resonance studies of amino acids and peptides, *J. Am. Chem. Soc.* 90 (14) (1968) 3738–3748.
- [42] E. Fleige, K. Achazi, K. Schaletzki, T. Triemer, R. Haag, Ph-responsive dendritic core-multishell nanocarriers, *J. Contr. Release* 185 (2014) 99–108.
- [43] Z. Xiao, Z. Su, S. Han, J. Huang, L. Lin, X. Shuai, Dual ph-sensitive nanodrug blocks pd-1 immune checkpoint and uses t cells to deliver nf- κ b inhibitor for antitumor immunotherapy, *Sci. Adv.* 6 (6) (2020), eaay7785.
- [44] Q.X. Teng, Y.V. Ashar, P. Gupta, E. Gadee, Y.F. Fan, S.E. Reznik, J.N.D. Worpel, Z. S. Chen, Revisiting mtor inhibitors as anticancer agents, *Drug Discov. Today* 24 (10) (2019) 2086–2095.
- [45] D.H. Ki, F. Ooppel, A.D. Durbin, A.T. Look, Mechanisms underlying synergy between DNA topoisomerase i-targeted drugs and mtor kinase inhibitors in nf1-associated malignant peripheral nerve sheath tumors, *Oncogene* 38 (39) (2019) 6585–6598.
- [46] P. Maiso, Y. Liu, B. Morgan, A.K. Azab, P. Ren, M.B. Martin, Y. Zhang, Y. Liu, A. Sacco, H. Ngo, F. Azab, P. Quang, S.J. Rodig, C.P. Lin, A.M. Roccaro, C. Rommel, I.M. Ghobrial, Defining the role of torc1/2 in multiple myeloma, *Blood* 118 (26) (2011) 6860–6870.
- [47] C.J. Norbury, B. Zhivotovsky, DNA damage-induced apoptosis, *Oncogene* 23 (16) (2004) 2797–2808.
- [48] R. Agami, R.J.C. Bernards, Distinct initiation and maintenance mechanisms cooperate to induce g1 cell cycle arrest in response to DNA damage, *Cell* 102 (1) (2000) 55–66.
- [49] L.J. Mah, A. El-Osta, T.C. Karagiannis, Gammah2ax: a sensitive molecular marker of DNA damage and repair, *Leukemia* 24 (4) (2010) 679–686.
- [50] J. Xu, L. Xu, C. Wang, R. Yang, Q. Zhuang, X. Han, Z. Dong, W. Zhu, R. Peng, Z. Liu, Near-infrared-triggered photodynamic therapy with multitasking upconversion nanoparticles in combination with checkpoint blockade for immunotherapy of colorectal cancer, *ACS Nano* 11 (5) (2017) 4463–4474.
- [51] Z. Zhang, B. Li, L. Xie, W. Sang, H. Tian, J. Li, G. Wang, Y. Dai, Metal-phenolic network-enabled lactic acid consumption reverses immunosuppressive tumor microenvironment for sonodynamic therapy, *ACS Nano* 15 (10) (2021) 16934–16945.
- [52] Z. Zhang, W. Sang, L. Xie, W. Li, B. Li, J. Li, H. Tian, Z. Yuan, Q. Zhao, Y. Dai, Polyphenol-based nanomedicine evokes immune activation for combination cancer treatment, *Angew. Chem. Int. Ed.* 60 (4) (2021) 1967–1975.
- [53] R.H. Fang, C.-M.J. Hu, B.T. Luk, W. Gao, J.A. Copp, Y. Tai, D.E. O'Connor, L. Zhang, Cancer cell membrane-coated nanoparticles for anticancer vaccination and drug delivery, *Nano Lett.* 14 (4) (2014) 2181–2188.
- [54] C.A. Janeway Jr., K. Bottomly, Signals and signs for lymphocyte responses, *Cell* 76 (2) (1994) 275–285.
- [55] J.R. Mora, M. Iwata, B. Eksteen, S.-Y. Song, T. Junt, B. Senman, K.L. Otipoby, A. Yokota, H. Takeuchi, P.J.S. Ricciardi-Castagnoli, Generation of gut-homing igasecreting b cells by intestinal dendritic cells, *Science* 314 (5802) (2006) 1157–1160.
- [56] R.S. Herbst, J.-C. Soria, M. Kowanzet, G.D. Fine, O. Hamid, M.S. Gordon, J. A. Sosman, D.F. McDermott, J.D. Powderly, S.N. Gettinger, Predictive correlates of response to the anti-pd-1 antibody mpd3280a in cancer patients, *Nature* 515 (7528) (2014) 563–567.
- [57] H. Luo, L. Kong, F. Zhang, C. Huang, J. Chen, H. Zhang, H. Yu, S. Zheng, H. Xu, Y. Zhang, Light-controlled nanosystem with size-flexibility improves targeted retention for tumor suppression, *Adv. Funct. Mater.* 31 (27) (2021), 2101262.
- [58] D.W. Zheng, Y. Chen, Z.H. Li, L. Xu, C.X. Li, B. Li, J.X. Fan, S.X. Cheng, X.Z. Zhang, Optically-controlled bacterial metabolite for cancer therapy, *Nat. Commun.* 9 (1) (2018) 1680.
- [59] D. Mossman, S. Park, M.N. Hall, Mtor signalling and cellular metabolism are mutual determinants in cancer, *Nat. Rev. Cancer* 18 (12) (2018) 744–757.
- [60] J.L. Yecies, B.D. Manning, Transcriptional control of cellular metabolism by mtor signaling, *Cancer Res.* 71 (8) (2011) 2815–2820.
- [61] D.-F. Lee, H.-P. Kuo, C.-T. Chen, J.-M. Hsu, C.-K. Chou, Y. Wei, H.-L. Sun, L.-Y. Li, B. Ping, W.-C. Huang, Ikk β suppression of tsc1 links inflammation and tumor angiogenesis via the mtor pathway, *Cell* 130 (3) (2007) 440–455.
- [62] K. Inoki, M.N. Corradetti, K.-L. Guan, Dysregulation of the tsc-*mtor* pathway in human disease, *Nat. Genet.* 37 (1) (2005) 19–24.
- [63] A. Giaccia, B.G. Siim, R.S. Johnson, Hif-1 as a target for drug development, *Nat. Rev. Drug Discov.* 2 (10) (2003) 803–811.
- [64] D. Gorenshyeyn, E. Zaslavsky, M. Fribourg, C.Y. Park, A.K. Wong, A. Tadych, B. M. Hartmann, R.A. Albrecht, A. Garcia-Sastre, S.H. Kleinstein, O.G. Troyanskaya, S. C. Sealfon, Interactive big data resource to elucidate human immune pathways and diseases, *Immunity* 43 (3) (2015) 605–614.
- [65] H. Zhu, J. Guo, Y. Shen, W. Dong, H. Gao, Y. Miao, C. Li, Y. Zhang, Functions and mechanisms of tumor necrosis factor- α and noncoding rnas in bone-invasive pituitary adenomas, *Clin. Cancer Res.* 24 (22) (2018) 5757–5766.